Experimental measurement of enhanced and hindered particle settling in turbulent gas-particle suspensions, and geophysical implications

Baptiste Penlou[1], Olivier Roche[1], Michael Manga[2], Siet van den Wildenberg[1,3]

[1]Université Clermont Auvergne, CNRS, IRD, OPGC, Laboratoire Magmas et Volcans, Clermont-Ferrand, F-63000, France
[2]Department of Earth and Planetary Science, University of California, Berkeley, CA, USA
[3]Université Clermont Auvergne, CNRS/IN2P3, Laboratoire de Physique de Clermont, Clermont-Ferrand, F-63000,France

Key Points:

- We investigate the relationship between particle concentration and particle settling velocity in turbulent air-particle mixtures.
- We demonstrate an interplay between hindered settling and cluster-induced enhanced settling, depending on the Stokes number.
- Clustering of 78 μm particles increases mean settling velocity, while 467 μm particles experience hindered settling.

Corresponding author: Siet van den Wildenberg, siet.van_den_wildenberg@uca.fr

Abstract

The dynamics of geophysical dilute turbulent gas-particles mixtures depends to a large extent on particle concentration, which in turn depends predominantly on the particle settling velocity. We experimentally investigate air-particle mixtures contained in a vertical pipe in which the velocity of an ascending air flux matches the settling velocity of glass particles. To obtain local particle concentrations in these mixtures, we use acoustic probing and air pressure measurements and show that these independent techniques yield similar results for a range of particle sizes and particle concentrations. Moreover, we find that in suspensions of small particles (78 μm) the settling velocity increases with the local particle concentration due to the formation of particle clusters. These clusters settle with a velocity that is four times faster than the terminal settling velocity of single particles, and they double settling speeds of the suspensions. In contrast, in suspensions of larger particles (467 μm) the settling velocity decreases with increasing particle concentration. Although particle clusters are still present in this case, the settling velocity is decreased by 30%, which is captured by a hindered settling model. These results suggest an interplay between hindered settling and cluster-induced enhanced settling, which in our experiments occur respectively at Stokes number O(100) and O(1). We discuss implications for volcanic plumes and pyroclastic currents. Our study suggests that clustering and related enhanced or hindered particle settling velocities should be considered in models of volcanic phenomena and that drag law corrections are needed for reliable predictions and hazard assessment.

Plain Language Summary

The propagation of turbulent dust storms, snow surge avalanches, dilute pyroclastic density currents, and volcanic plumes is controlled by the particle concentration, which depends on the particle settling velocity. Most numerical models consider only theoretical single-particle settling velocities. However, in the presence of neighboring particles, the settling velocity is strongly affected by gas-particle and particle-particle interactions. Our main objective is to unravel the relationship between the particle concentration and the particle settling velocity. We present laboratory experiments, in which the local particle concentration is measured using two independent techniques. We observe two settling mechanisms depending on the coupling of the particles with the gas, namely, hindered settling or cluster-induced enhanced settling. These mechanisms result in settling velocities significantly different from those of single particles. As an illustrative example, we consider the fall deposit of the 10.5 ka Plinian eruption at Llaima (Chile) and argue that clusters of centimeter-sized clasts had enhanced settling velocities similar to those of 10-20 cm diameter clasts. Our main conclusion is that mechanisms causing enhanced or hindered particle settling velocities should be considered for accurate models of geophysical processes, possibly through drag law corrections.

1 Introduction

Dust storms, snow surge avalanches, dilute pyroclastic density currents, and volcanic plumes are examples of geophysical flows of particles in a turbulent gas. The settling velocity of particles is essential because it controls the particle concentration and hence the dynamics of these flows. If the particles are suspended by the fluid, the dynamics of the mixture is controlled by the coupling of the fluid and the particles as well as interparticle collisions. Instead, if the particles are not suspended, they settle to form a deposit or a dense basal flow controlled by particle-particle interactions. Experimental and numerical studies revealed that the particle settling velocity may increase (Wang & Maxey, 1993; Dey et al., 2019) or decrease (Nielsen, 1993; Fornari et al., 2016; Dey et al., 2019) depending on the degree of turbulence, and it can be lower (Marchetti et al., 2022) or higher (Del Bello et al., 2017) than predicted theoretically for a single par-

ticle depending on the particle size, shape, and concentration. Actual particle settling velocities different from theoretical velocities used in models may be a cause of discrepancies between observed and simulated volcanic fall deposits (Tadini et al., 2020, 2022) and this issue is critical in the context of hazard assessment.

Dilute turbulent gas-particle mixtures are known to exhibit regions of higher particle concentrations called clusters, which affect the mixture dynamics and the particle settling velocity (Fullmer & Hrenya, 2017; Brandt & Coletti, 2022). The key mechanisms that lead to particle clustering can be divided into two categories: dissipation of granular temperature (i.e., fluctuations in particle velocities) due to inter-particle collisions, and relative motion between the particles and the continuous fluid. Only a few numerical and experimental studies have addressed the effects of clustering on the particle settling velocity and they revealed that clusters had a fall velocity greater than that of a single particle (Wang & Maxey, 1993; Uhlmann & Doychev, 2014; Breard et al., 2016; Fornari et al., 2019; Fong & Coletti, 2022). In this context, recent experiments showed that the lifespan of clusters in mixtures of particles suspended by an ascending air flow played a fundamental role in setting a critical concentration of particles above which additional particles were not maintained in the mixtures (Weit et al., 2019; van den Wildenberg et al., 2020; Fong & Coletti, 2022).

How clustering controls the particle settling velocity and the dynamics of dilute turbulent geophysical flows remains an open question. The major challenge to addressing this issue experimentally is to obtain reliable values for the solid volume fraction inside 3D suspensions and over a range of controlling parameters. This is due the relatively large size of the particles ($\sim$100 μm) and their concentration ($\sim$0.1-10 vol.%), which results in scattering of light and makes optical observation complicated (Fong & Coletti, 2022). Therefore, experimental studies are often restricted to very dilute suspensions with particle concentrations $\ll$ 1 vol.% (Fong & Coletti, 2022; Del Bello et al., 2017) in which particle-fluid (two-way) interactions are expected to dominate. In the present study, we use two independent techniques to investigate particle settling in suspensions with particle concentrations $\sim$0.1-3 vol.%: acoustic probing (van den Wildenberg et al., 2020) and local pressure measurements. We quantify the relationship between the settling velocity (i.e., the flow velocity necessary to suspend the particles) and the concentration of particles. We find that the settling velocity in suspensions of 78 μm particles with Stokes number O(1) increases with the local particle concentration and is higher than that of a single particle, hence revealing enhanced settling. In contrast, suspensions of 467 μm particles with Stokes number O(100) experience hindered settling. We discuss implications of our results for geophysical flows, focusing on volcanic mixtures generated by explosive eruptions.

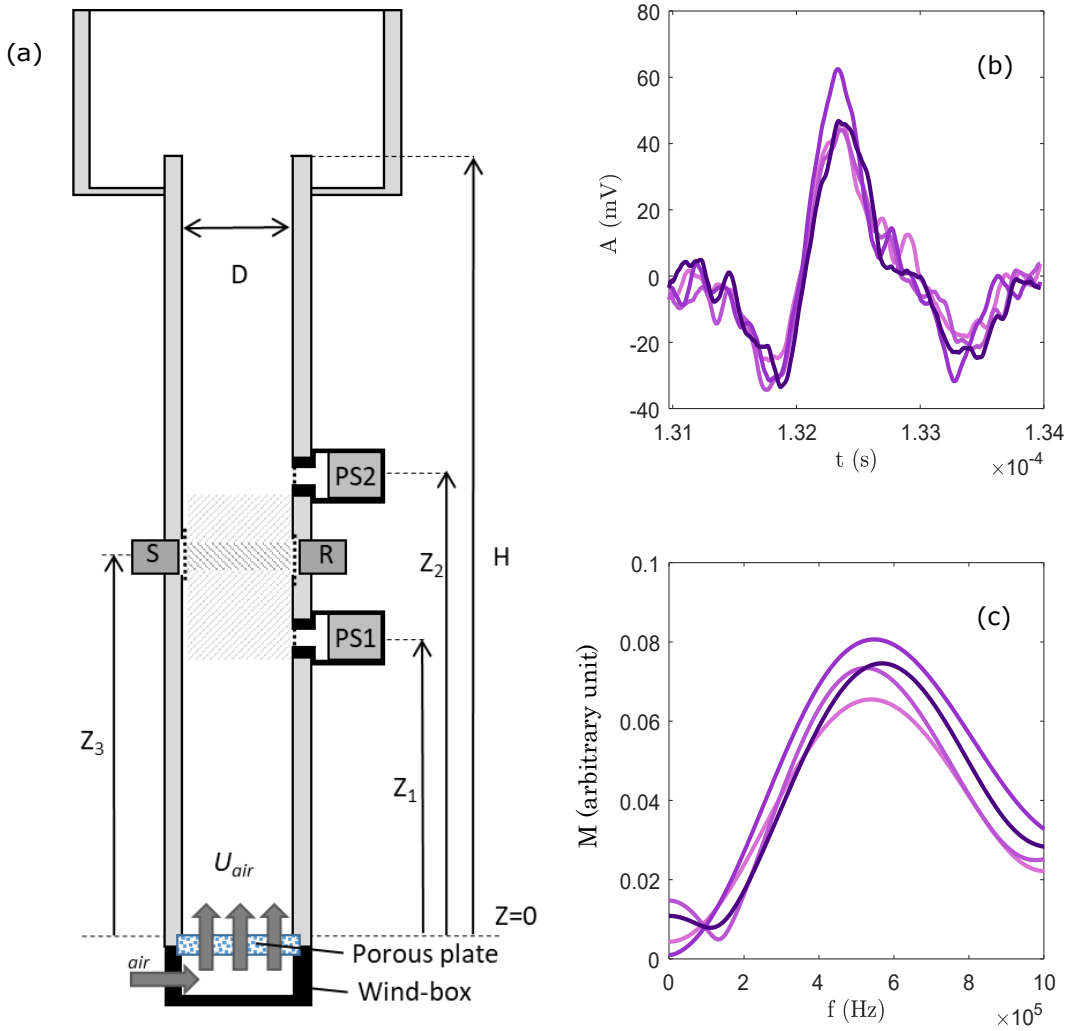


Figure 1. (a) The experimental setup is a cylindrical pipe of height H= 1 m and inner diameter D= 4 cm. An air flow is delivered into the container via a wind-box and a porous plate, and a large cylinder at the top of the pipe allows the air velocity to decrease. Interstitial air pressure is measured by two piezo-resistive sensors (PS) placed at heights Z_1= 51.5 cm and Z_2= 56.5 cm. Two piezo-electric transducers (S and R) placed at position Z_3= 54 cm (in between PS_1 and PS_2) are used to measure acoustic wave propagation through the suspension. The volume probed by the local fluid pressure measurements is depicted in dashed light grey, and the volume probed by the acoustic monitoring is depicted in dashed dark grey. (b) Amplitude versus time for four typical (coherent) sound waves measured in different suspensions of glass particles with d= 467 μm and $\phi_L \sim$ 1 %. Here t= 0 corresponds to the time at which the ultrasonic pulse is sent by the source transducer. (c) Magnitude versus frequency obtained from fast Fourier transforms of the four the sound waves in (b).

2 Methods

2.1 Experimental device and material

All experiments were performed at room temperature in a cylindrical pipe with a height (H) of 1 m and an inner diameter (D) of 4 cm (Fig. 1). At the base of the pipe

is a porous plate and the ensemble is placed on a wind-box. It was shown that the geometry of the air inlet is important for the stability of the air flow (Bagheri et al., 2013; Bonadonna & Phillips, 2003) and, therefore, the wind-box has the same inner diameter as the pipe. An air supply system delivered mean air flow velocities (U) through the wind-box and the porous plate into the pipe. For particle sizes smaller than 300 μm, we used the compressed air available in the laboratory and set the air flow using debit controllers that had a precision of less than 1 L/min. For particle sizes larger than 300 μm, a compressor (Worthington Creyssensac RLR 35B) was used in combination with a dedicated debit controller. This controller had a minimum increment of 10 L/min (with a precision of about 2 L/min). The porous plate had a thickness of 10 mm and a pore size of 20 μm. The influence of the porous plate on the turbulent structures of the airflow is not trivial. We expect that when the air exits the plate the eddy size will be roughly equal to the size of the pores, and the eddy size grows -as the air flows upwards in the pipe- to about half the pipe's diameter.

At the top of the pipe, a large diameter cylinder ($\sim 2D$) allowed the air velocity to decrease and prevented the loss of particles from the pipe. The pressure of the interstitial air was measured by two piezo resistive sensors installed at heights Z_1= 51.5 cm and Z_2= 56.5 cm above the porous plate. The sensors were placed in adapters, which were in direct contact with the suspension via a small hole covered by a grid (36 μm mesh size) to prevent particles entering the adapter and colliding with the sensor. Furthermore, two piezo-electric transducers placed at position Z_3= 54 cm (in between pressure sensors PS_1 and PS_2) were used to measure acoustic wave propagation through the suspension. One transducer was used as an acoustic source (S) while the second transducer (R) detected the wave at a distance $L \sim 0.04$ m from the source. To avoid pollution of the acoustic signal by particles colliding against the transducer-face, 36 μm mesh size grids were installed on the inside wall of the container in front of the transducers. A typical experiment is performed as follows. First, a known mass of glass beads is poured into the pipe, and a mean input solid volume fraction ϕ_i is calculated from the mass and the assumption that the beads are homogeneously distributed over the volume of the cylinder. Then, the particles are suspended in air by a vertical upward air flux at velocity U and the fluid pressure is measured using the two pressure sensors. Additionally, 400 short pulses are sent by a piezo-electric transducer and the propagating pulses are measured. For each particle size, the experiment is repeated 3 times. We experimented with nearly mono disperse spherical glass particles with density $\rho_2 \sim 2500$ kg/m^3 and mean diameters d of 49, 78, 206, 308 and 467 μm (sieved between: 45-53, 75-80, 200-212, 300-315, 450-475 μm, respectively). We filmed the suspensions with a high-speed Photron Fastcam SA3 video camera, with resolution of 0.77 mm per pixel, located at 30 cm from the pipe. Movies were acquired at a rate of 250 frames per second and a spatial resolution of 58 x 882 pixels. Improved contrast was achieved by placing the pipe about 50 cm in front of a 40 W white light panel of size 59.5 x 59.5 cm, of which 54.4 x 54.4 cm was the lighting surface.

2.2 Interstitial fluid pressure data

Interstitial fluid pressure arises from air-particle differential motion and the related drag. In each experiment, the generated fluid pressure is measured over time using the pressure sensors that take 500 samples each with a sampling rate of ∼50 Hz. The bulk solid volume fraction above each sensor may be obtained from the time-averaged pressure (P) via: $\phi_b = P/(\rho_2 g(H - Z_i))$ (Weit et al., 2019). However, this implies that the suspension is homogeneous, which is not necessarily true. Therefore, in this study we calculate a local solid volume fraction from the pressure measurements of two pressure sensors (PS$_1$ and PS$_2$), as follows: $\phi_L = \Delta P/(\rho_2 g \Delta Z)$ with $\Delta P = P_1 - P_2$ and $\Delta Z = Z_2 - Z_1 = 5$ cm (the indices indicate the pressure sensors) and the volume probed is depicted in Fig. 1. From $\phi_L(t)$ it can be observed that a quasi steady state is attained (see Supplementary Information section 1), and only for the smaller particles do we ob-

Table 1: Symbols and their units

Symbol	Units	Definition
C_d	-	Drag coefficient for a single particle
d	μm	Particle diameter
D	m	Inner diameter of pipe
H	m	Height of pipe
U	m.s^{-1}	Mean air flow velocity
U^*	m.s^{-1}	Mean particle settling velocity in the suspension
U_m	m.s^{-1}	Air velocity corresponding to ϕ_{Lm}
U_t	m.s^{-1}	Terminal settling velocity of a single particle
$U_{cluster^*}$	m.s^{-1}	Reduced cluster velocity (velocity in laboratory reference frame)
$U_{cluster}$	m.s^{-1}	Cluster velocity ($U_m + U_{cluster^*}$)
Re_p	-	Particle Reynolds number
St	-	Stokes number
T	s	Cluster lifetime
Z	m	Elevation in pipe
α	m^{-1}	Attenuation coefficient
β	-	Effective drag coefficient
η	Pa.s	Gas dynamic viscosity
κ_1	N.m^{-2}	Air compressibility
κ_1	N.m^{-2}	Solid compressibility
ρ_1	kg.m^{-3}	Air density
ρ_2	kg.m^{-3}	Solid density
ϕ	-	Particle volume fraction
ϕ_c	-	Maximum particle volume fraction that can be suspended
ϕ_i	-	Particle volume fraction assuming particles are homogeneously distributed in pipe
ϕ_L	-	Local particle volume fraction
ϕ_{Lm}	-	Maximum local particle volume fraction
k	m^{-1}	complex wavenumber
σ	-	density ratio

serve a small drift due to loss of particles during the experiment. A time averaged ϕ_L may thus be calculated by averaging the 500 samples ($\sim$ 10 s).

2.3 Acoustic measurements

In each experiment, we measure the propagation of 400 short acoustic pulses with central frequency f= 0.5 MHz and repetition time of 30 ms. For each transmitted signal, the frequency dependent attenuation coefficient $\alpha(f)$ is determined from the fast Fourier transform (FFT) using: $\alpha(f) = (-1/D)\ln(A_{sus}/A_f)$, with A_f and A_{sus} the amplitudes obtained from the FFT for acoustic signals propagating through a pure fluid phase (air) and the granular suspension, respectively. The attenuation coefficient spectra are averaged over all 400 pulses to obtain a mean attenuation spectrum for each experiment.

We interpret our experimental measurements with two models. For more details we refer readers to van den Wildenberg et al. (2020) and references therein.

(i) The coupled-phase hydrodynamic model developed by Urick (1948) considers a system with a volume fraction ϕ of solid particles with density ρ_2 and compressibility κ_2, suspended in a viscous continuous phase with density ρ_1 and compressibility κ_1. In the long wavelength limit ($\lambda/d \gg 1$), the ultrasound attenuation coefficient in such a system is approximated as (Urick, 1948):

$$\alpha = \phi\left[\frac{1}{6}k^4a^3 + k(\sigma-1)^2\frac{s}{s^2+(\sigma+\tau)^2)}\right] + \zeta \tag{1}$$

where $a = d/2$, the wavenumber $k = \omega/v$ with ω the angular frequency, $v \sim 349$ m/s the sound velocity in air, $\sigma = \rho_2/\rho_1$, $\tau = (1/2) + (9/4)(\delta/a)$, and $s = (9/4)[(\delta/a) + (\delta/a)^2]$. Here $\delta = \sqrt{2\eta/(\omega\rho_1)}$ is a characteristic viscous (shear wave) length, with η the dynamic viscosity of the continuous phase, and ζ is a frequency independent offset (van den Wildenberg et al., 2020).

(ii) The ECAH theory is based on scattering models at the microscopic scale ($\lambda/d \sim 1$) developed by Epstein and Carhart (1953) and Allegra and Hawley (1972). The model describes the interactions of scattered, visco-inertial, and thermal fields with a single particle and its surrounding medium (Epstein & Carhart, 1953; Allegra & Hawley, 1972; Ying & Truell, 1956; Challis et al., 2005). As the density contrast between the two phases (air and glass) is very high, we neglect the thermal contribution (Challis et al., 2005). Finally we combine the ECAH theory with a multiple scattering theory to correlate the complex wavenumber (k) to the frequency dependent α via:

$$\alpha = \zeta + Im\left[\sqrt{k^2 + \frac{3\phi}{a^3}f(0) + \frac{9\phi^2}{4a^6k^2}(F^2(0) - F^2(\pi))}\right] \tag{2}$$

Here Im signifies the imaginary part and $F(0)$ and $F(\pi)$ are the forward and backward scattering amplitudes of the individual particles, respectively. The scattering amplitudes are calculated from the scattering coefficients of the various types of waves scattered from an individual particle, and we consider scattering and viscous/inertial losses and neglect thermal conduction losses. ϕ is then calculated from the experimental acoustic data by fitting the theoretical α from the models using Matlab's least-squares curve fitting tools. In the dilute suspensions considered here, the additional free fitting parameter $\zeta \sim 0$-1.

3 Results

3.1 Acoustic probing and local fluid pressure measurements

We start by comparing the local solid volume fraction ϕ_L obtained by local fluid pressure measurements and acoustic attenuation measurements. To do so, we introduce a known mass of particles (d= 49, 78, 206, 307 or 467 μm) into the container and choose U so that ϕ_L obtained from the fluid pressure is about 1%. Then, we measure the propagation of 400 acoustic pulses. The similarity between the acoustic pulse signals demonstrates the reproducibility of the sound propagation through the suspension (Fig. 1b) and spectral analysis of the sound signals evidences a single peak around $f_c \sim 0.5$ MHz (Fig. 1c). The attenuation coefficient α, calculated from the spectral analysis, increases with the frequency (Fig. 2a). In order to infer ϕ_L we compare $\alpha(f)$ with existing theoretical models. For the particles smaller than 200 μm, both the Urick and ECAH models predict well the experimental data (Fig. 2a). In contrast, for the larger particles, only the ECAH model appears to be able to describe our data (Fig. 2a). For each particle size, a mean ϕ_L is calculated from the pressure measurements and from the acoustic monitoring by averaging 3 experiments. Importantly, we find overall a good agreement between ϕ_L obtained by the local fluid pressure and acoustic methods (Fig. 2b).

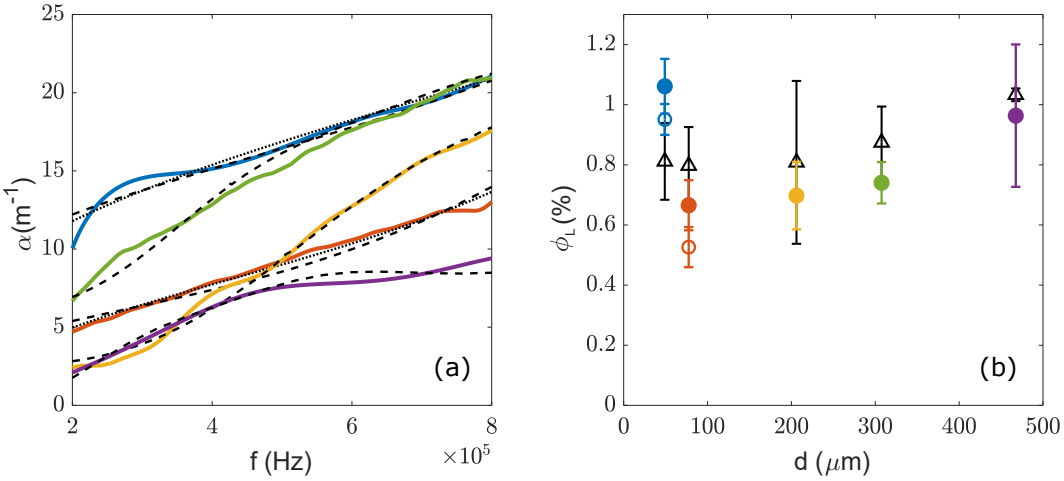


Figure 2. Acoustic wave attenuation in suspensions of glass beads. (a) Example traces of α versus frequency for suspension of glass particles in air (blue: d= 49 μm, orange: d= 78 μm, yellow: d= 206 μm, green: d= 308 μm, purple: d= 467 μm). The dotted lines represent the fits of $\alpha(f)$ by the Urick model (Eq.1). The dashed lines represent the fits of $\alpha(f)$ by the ECAH44 model (Eq.2). (b) ϕ_L averaged over 3 experiments as a function of the particle diameter. Solid dots represent ϕ_l obtained from the ECAH44 model, open dots represent ϕ_L obtained from the Urick model, and triangles represent the ϕ_L obtained from the local fluid pressure. The error bars show the standard deviations over the experiments. Colors correspond to those in (a).

To test the applicability of these techniques over a wider range of particle concentrations, a mass of particles of 160.08 g (corresponding to $\phi_i = 5\%$) is introduced into the container at U= 0. Subsequently U is slowly ramped-up and the acoustic wave propagation and the fluid pressure are measured. We use glass beads of size d= 78 μm and 467 μm, and the experiment is repeated 3 times. Traces of $\alpha(f)$ reveal that the sound attenuation increases with U as more particles enter the volume probed by the acoustic wave (Fig. 3a). Since the ECAH model appears to work for both particle sizes, we will use this model to infer ϕ_l from $\alpha(f)$. As before, we determine a mean ϕ_L for the pressure measurements and for the acoustic monitoring by averaging over all experiments. Figure 3b shows ϕ_L as a function of U. Overall, we find that ϕ_L obtained by the two techniques are similar for all the concentrations tested. For the particles d= 78 μm, ϕ_L is first nearly 0 for the lowest flow velocities, and above $U \sim 0.4$ m/s it increases until a maximum of $\phi_L \sim 0.5\%$ is reached at $U \sim 0.58$ m/s, above which ϕ_L decreases as the particles are dragged above the position of the sensors. For the suspensions of larger particles d= 467 μm, we observe a similar behavior, but for higher U. One important observation is that, even though the ϕ_i is the same (5%), the maximum ϕ_L obtained differs significantly for the two particle sizes. For the d= 467 μm particles we find that $\phi_L \sim$ 4% ($\sim \phi_i$), while for the d= 78 μm particles $\phi_L \sim 0.45\%$ almost ten times smaller than ϕ_i.

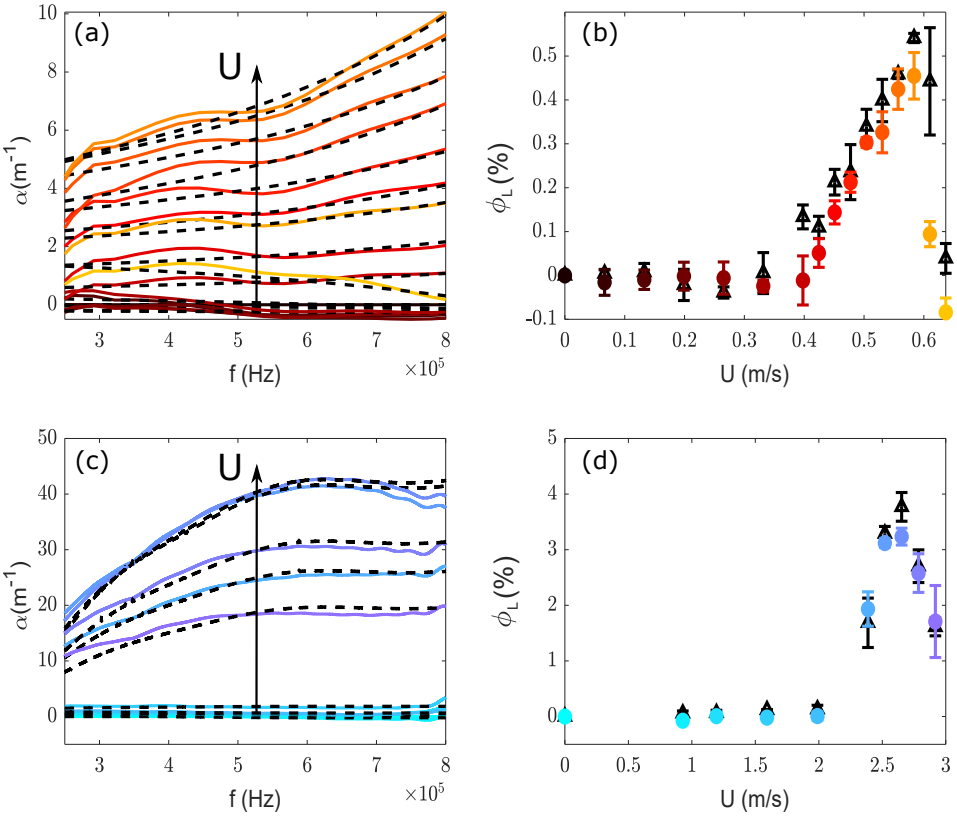


Figure 3. (a) Attenuation coefficients versus frequency in a suspension of d= 78 μm glass beads for increasing U. (b) ϕ_L obtained from fits of $\alpha(f)$ in (a) by the ECAH44 model (black dashed lines in a). The black triangles are ϕ_L obtained from local fluid pressure. (c) Same as (a) for d= 467 μm glass beads. (d) ϕ_L obtained from fits in (c) by the ECAH44 model (black dashed lines in c). The black triangles are ϕ_L obtained from the local fluid pressure. Error bars represent the standard deviations over three experiments.

3.2 Local solid volume fraction and clustering

Next, we investigate the relationship between the maximum local solid volume fraction ϕ_{Lm}, the air velocity, and the particle size. Experiments are repeated for varying ϕ_i and for simplicity we use only fluid pressure measurements to calculate ϕ_L. The resolution in the experiments is limited by the minimal increments of the flow meter, from which the error bars in U are determined. In suspensions of 78 μm particles, we find that, for a given ϕ_i, ϕ_L increases with U to ϕ_{Lm} at U_m, after which it decreases rapidly (Fig. 4a). Importantly, for increasing ϕ_i, both the ϕ_{Lm} and U_m increase (Fig. 4c,d). For the suspensions of 467 μm particles, a similar behavior is found for ϕ_L and ϕ_{Lm}, with ϕ_L increasing with U until its maximum value ϕ_{Lm} at U_m, and increasing ϕ_i leads to a higher ϕ_{Lm} (Fig. 4b,e). However, in contrast to the smaller particles, U_m appears to decrease with increasing ϕ_i (Fig. 4f).

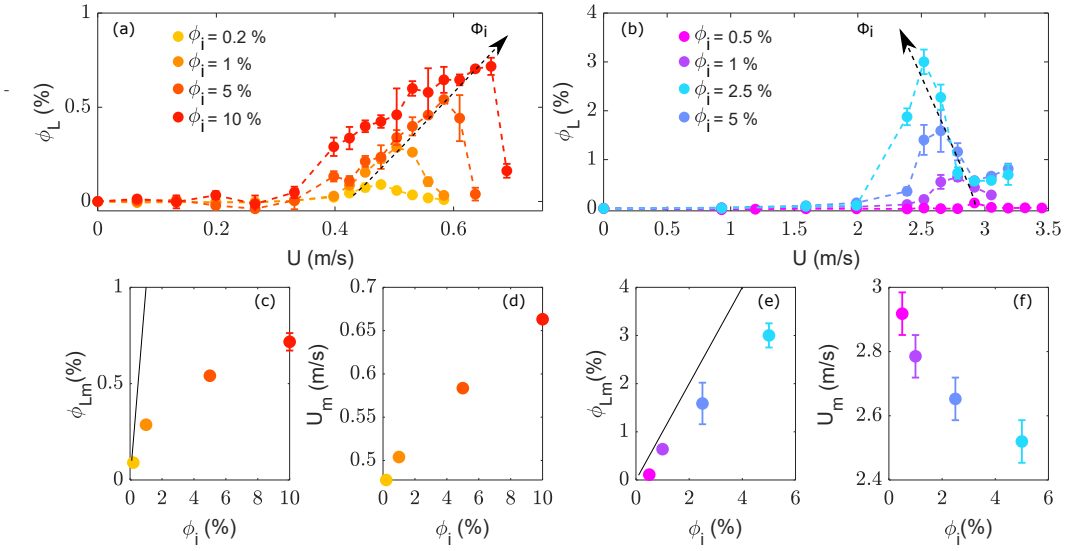


Figure 4. ϕ_L calculated from local pressure measurements and presented as a function of the air velocity U. (a) Suspensions of d= 78 μm glass for increasing ϕ_i [ϕ_i= 0.2% (yellow), 1% (light orange), 5% (dark orange), 10% (red)]. The dashed arrow illustrates the shift of the curves to the right for increasing ϕ_i. (b) Suspensions of d= 467 μm glass beads [ϕ_i= 0.5% (magenta), 1% (dark purple), 2.5% (light purple), 5% (blue)]. The dashed arrow illustrates the shift of the curves to the left for increasing ϕ_i. (c) The maximum local concentration ϕ_{Lm} versus ϕ_i from the data in (a). The line represents $\phi_{Lm} = \phi_i$. (d) The air velocity U_m corresponding to ϕ_{Lm} versus ϕ_i from the data in (a). (e) The maximum local concentration ϕ_{Lm} versus ϕ_i from the data in (b), the line represents $\phi_{Lm} = \phi_i$. (f) The air velocity U_m corresponding to ϕ_{Lm} versus ϕ_i from the data in (b). Error bars of ϕ are the standard deviations over the experiments, error bars in U_m are the increment in the air velocity (for the d= 78 μm particles the error bars of U_m are the size of the symbols).

We filmed each suspension at ϕ_{Lm} and the corresponding U_m, focusing on the region between PS_1 and PS_2. Frames from those movies are presented in Fig. 5 and show that regions with high particle concentrations (clusters) are present in all the suspensions, except in those with the lowest ϕ_{Lm}. This supports the idea that cluster lifespan plays an important role in the maximal concentration of particles that can be suspended (ϕ_c) as well as in the formation of dense beds at the bottom of the suspension (van den Wildenberg et al., 2020; Fong & Coletti, 2022).

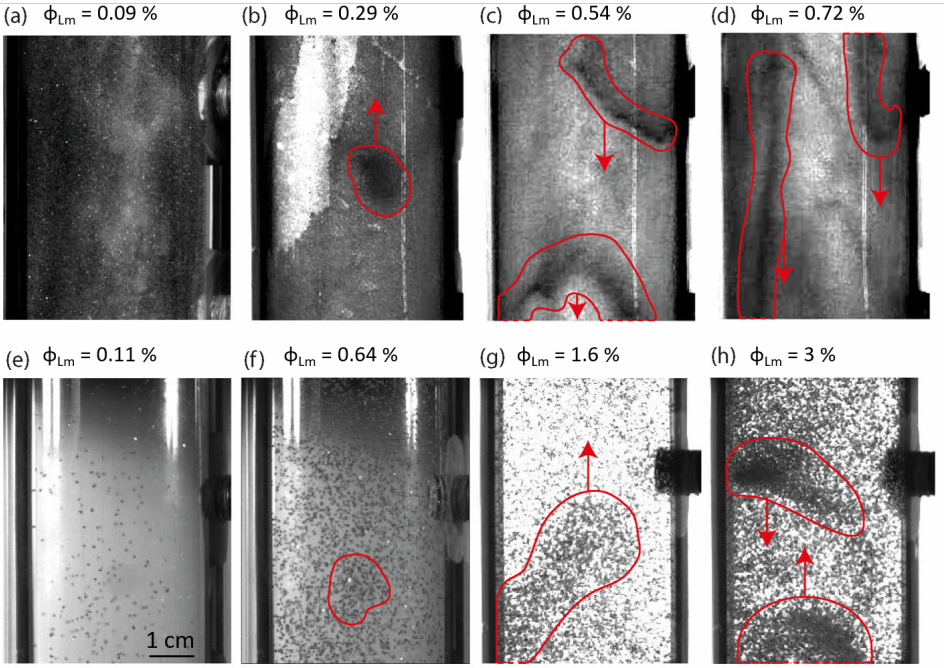


Figure 5. Frames from movies of suspensions with varying ϕ_i at the relevant U_m. The movies are focused on the region between pressure sensors PS_1 and PS_2. (a)-(d) suspensions of 78 μm particles with ϕ_{Lm}= 0.09, 0.29, 0.54 0.72%, respectively. (e)-(h) suspensions of 467 μm particles with ϕ_{Lm}= 0.11, 0.64, 1.6, 3%, respectively. Particles are black against a white background, except for in (a) where the particles are white against a black background. Denser regions of particles are outlined in red and the arrows indicate the direction of cluster movement.

A detailed investigation of the size, shape, and particle concentration of clusters is beyond the scope of this paper due to the spatial resolution of the images and is further complicated by the limited penetration of the light through the suspension. We thus provide a phenomenological description of the suspensions. Clusters in the suspensions of small particles tend to be elongated and relatively concentrated by comparison to clusters observed in the suspension of larger particles which are more rounded and less concentrated (Fig.5). In circulating fluidized bed risers (with higher particle concentrations compared to our experiments), cluster size shows no systematic variations with the particle size nor the riser size (Cahyadi et al., 2017; Berruti et al., 1995).Instead, it has been shown to, in some cases, vary with the radial position due to variations in radial velocity as particles go up in the middle and down on the sides (Cahyadi et al., 2017; Berruti et al., 1995). Our experiments show similar cluster trajectories (Supplementary Information section 4 and supplementary movies), however, variations in cluster size remain elusive. These are qualitative impressions and care should be taken when interpreting 2D projections of 3D structures.

In order to accurately determine the cluster fall velocity ($U_{cluster}$), it is necessary to consider long trajectories. Therefore, we filmed the suspensions of d = 78 μm particles at ϕ_L = 0.7% and U_m = 0.66 m/s, and d = 467 μm particles at ϕ_L = 3% and U_m = 2.5 m/s, imaging the whole pipe at a frame rate of 250 Hz (see Supplementary movies). The duration of those movies corresponds to the time over which a pressure measurement was performed. Small particles are lost during the time of the movie, which results in progressively lighter images. However, this loss is small and does not change significantly ϕ_L. To study the motion of the clusters we first produce a kymograph, which

is an intuitive way to represent the dynamics of the clusters during the movie in a single image. For each image of the movie, we plot the light intensity along a line in the Z-direction near the center of the pipe (Fig. 6). Clusters that ascend and descend are depicted in the kymograph as trajectories with a positive slope and a negative slope, respectively. The trajectories of these clusters show that their motion is mostly smooth and continuous. We thus determine the slope and length of the trajectories corresponding to the settling velocity $U_{cluster^*}$ and lifetime T of the clusters. Note that $U_{cluster^*}$ is a reduced settling velocity owing to the ascending air flow. We use ImageJ and the available plugin *RidgeDetection* (Steger, 1998), which is an algorithm developed for detecting ridges and lines. We consider trajectories with a minimal length of 70 frames (corresponding to 0.28 s), so that their slope is well defined. We find that the identified trajectories converge for 78 μm particles with parameters linewidth= 3, lower threshold = 0.2 and upper threshold = 1.4. For 467 μm particles, a linewidth=3, lower threshold = 0.2 and upper threshold=7.1 are used. For each movie, we track about 140 descending clusters and show the results in histograms in Fig. 6b,c. Descending clusters appear significantly more numerous (more than 70% of the clusters descend, see Fig.6e) and in general we have the impression that they are more concentrated than ascending clusters (Supplementary movies).The average lifetime of clusters is about 0.6 s and is the same in suspensions of 78 μm particles and in suspensions of 467 μm particles. However, the mean settling velocity of descending clusters, as determined from averaging all positive $U_{cluster^*}$ for a given particle size, in suspension of 78 μm particles is $\bar{U}_{cluster^*} \sim 0.9$ m/s, while in suspensions of 467 μm particles we find that $\bar{U}_{cluster^*} \sim 1.1$ m/s.

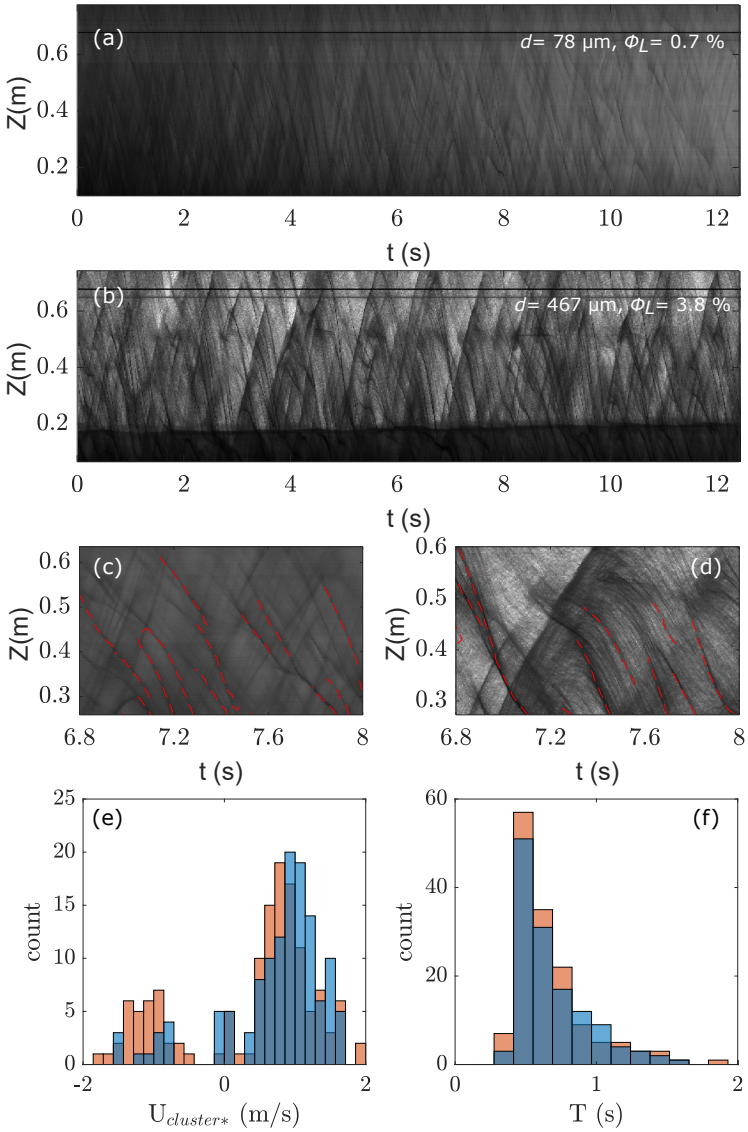


Figure 6. Kymographs of clusters in suspensions of (a) d= 78 μm particles, and, (b) d= 467 μm particles. (c and d) Zoom of the kymograph in (a) and (b), trajectories of clusters are shown by the red dashed lines. (e) Histogram of the reduced velocities of tracked clusters. Negative velocities correspond to ascending clusters, while positive velocities correspond to descending clusters. Most of the tracked clusters descend. (f) Histogram of lifetime (T) of descending clusters. Red and blue (transparent) colors correspond to suspensions of 78 μm and 467 μm particles, respectively.

4 Discussion

4.1 Acoustic probing and local fluid pressure measurements

The solid volume fraction in particle suspensions is difficult to measure experimentally. Our first main result is the comparison of two independent approaches to determine the local solid volume fraction (ϕ_l) in dilute but optically opaque suspensions of particles in air, namely (i) local fluid pressure measurements and (ii) acoustic probing. These techniques yield similar local solid volume fractions for a wide range of particle

sizes and particle concentrations. They thus present tools for investigating the solid volume fraction in laboratory experiments. Local fluid pressure measurements have the advantage that they offer ready access to the local solid volume fraction, without the need of many additional parameters such as, for example, the particle size or the viscosity of the fluid. Its main limitation is that it can be used only when there is a significant interstitial fluid pressure. Instead, acoustic monitoring can be used in the absence of fluid pressure. It is, however, more laborious to apply and needs more physical parameters, which may not be known. Moreover, in suspensions of particles larger than 200 μm the Urick model yields poor fits with unreasonably low ϕ_L indicating that this model fails. Under the assumption that the viscosity/inertia is responsible for the acoustic energy loss, only the second term in Eq. 1 (viscous-inertial loss) may be used (Pierce et al., 2016). Indeed, the use of only this term captures our data $\alpha(f)$ for the larger particles. However, the inferred $\phi_L \sim$ 3-4% is larger than the $\sim$ 1% obtained from the ECAH model and from local pressure measurements (Supplementary Information section 2). Further work is needed to address this issue.

4.2 Local solid volume fractions and particle settling velocities

The second main result is the dependence of U_m on the maximum local particle concentration ϕ_{Lm}, as observed in Fig. 4a&b, and for clarity we present cross plots in Fig. 7a&c. For the 78 μm particles, U_m increases rapidly with increasing ϕ_{Lm} (Fig.7a), indicating that these particles settle faster at higher particle concentrations. Instead, for the 467 μm particles, U_m decreases with increasing ϕ_{Lm} (Fig.7c), indicating that these larger particles settle slower at higher concentrations. In the following sub-sections we will discuss these findings in detail.

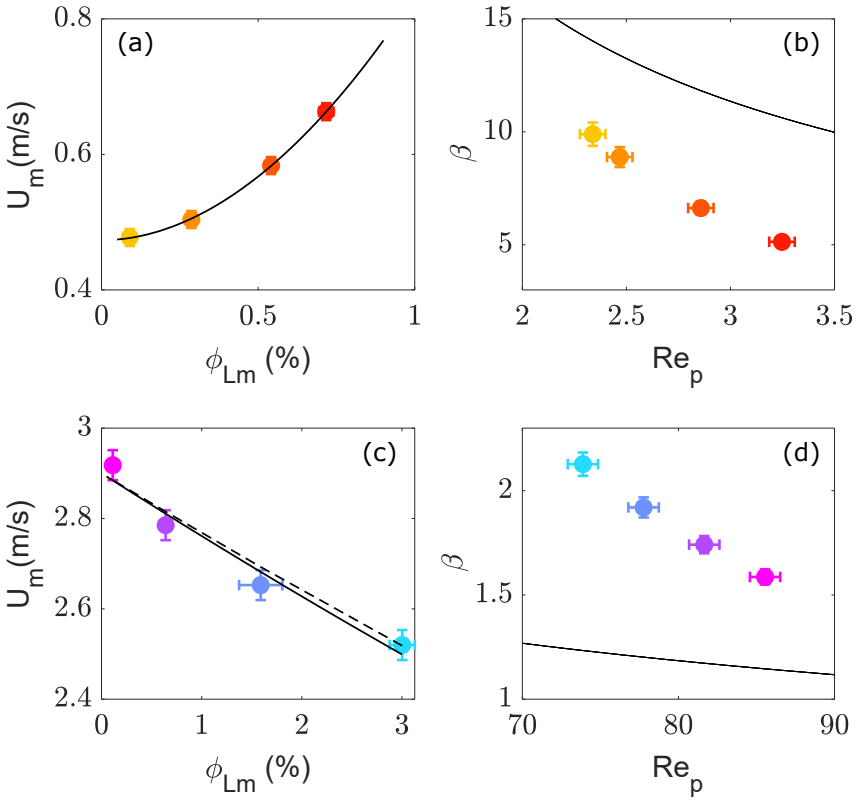


Figure 7. (a) Cross-plots of U_m versus ϕ_{lm} for suspensions of 78 μm particles (data from Fig. 4a). The solid black curve is a power law fit. (b) Effective drag coefficient β calculated from (a) versus the Re_p. The black curve is the estimated drag on a single particle via Abraham's contribution. (c) Cross-plot of U_m versus ϕ_{lm} (data from Fig. 4b) for suspensions of 467 μm particles. Solid black curves are fits of $U_m = p_1(1-\phi_{Lm})^{p_2}$ and theoretical predictions using $U^* = p_1(1-\phi)^n$ with $n = (5.1 + 0.27Re_p^{0.9})/(1 + 0.1Re_p^{0.9})$ (dashed curve). (d) β calculated from (c) versus the Re_p. The black curve is the estimated drag on a single particle via Abraham's contribution (see main text).

4.2.1 Air flow regime

The hydrodynamics of the macroscopic air flow in our device is described by the Reynolds number $Re = \rho_1 U_m D/\eta$. For the suspensions of 78 μm particles at $U_m \sim 0.6$ m/s we obtain $Re \sim 1500$, corresponding to a laminar flow, while for the suspensions of 467 μm particles at $U_m \sim 2.7$ m/s we obtain $Re \sim 6800$, corresponding to a turbulent flow. Note that in the experiments, the presence of particles in the fluid significantly complicates the flow dynamics with respect to those in pure fluid (Tsuji et al., 1984; Jessop & Jellinek, 2014).

The motion of a spherical particle falling through a fluid is controlled by two dimensionless numbers, $\sigma = \rho_2/\rho_1$ and the particle Reynolds number Re_p. The local flow around the particle may be estimated via $Re_p = \rho_1 dU/\eta$, where $\rho_1 = 1.13$ kg/m^3 and $\eta = 1.81\times10^{-5}$ kg/(m s) are the density and dynamic viscosity of air, respectively. For the suspension of 78 μm particles, with U_m varying from 0.4 to 0.7 m/s, this gives a $Re_p \sim$ 1.9-3.4. For the suspensions of 467 μm particles, taking $U_m \sim$ 2.5-3 m/s, this gives Re_p ranging from 73-88. The obtained Re_p indicates that all the suspensions studied here are in the transitional flow regime ($1 < Re_p < 1000$) (Rhodes, 2008).

4.2.2 Effective drag coefficient β

Consider a single particle in a suspension and suppose that U_m is equal and opposite in direction to its fall velocity. Ignoring fluid inertia, there are three forces acting on the particle, a buoyancy force, a gravitational force and a drag force F_d, so that: $\pi d^3(\rho_2-\rho_1)g/6 = F_d$, where $F_d = (1/2)\rho_1 A U_m^2 \beta$, with A the surface of the sphere on which the drag acts and β the effective drag coefficient. The drag coefficient is calculated from

$$\beta = dg(4/3)(\rho_2/\rho_1 - 1)/U_m^2 \tag{3}$$

and shown as a function of Re_p in Fig. 7b,d. We find that β is a decreasing function of Re_p similar to the drag coefficient for single particle, C_d, estimated by the Abraham contribution in the transitional flow regime $C_d = [0.5407+(24/Re_p)^{1/2}]^2$ (Abraham, 1970). Additionally, we find that for suspensions of small particles, $\beta < C_d$, while for suspensions of larger particles, $\beta > C_d$. This suggests that different mechanisms control the settling dynamics in suspensions of smaller particles and larger particles, as discussed below.

4.2.3 Hindered settling

Particles falling in a particle-laden fluid experience a larger fluid drag than a particle falling in a pure fluid due to the flow around neighbouring falling particles, an effect called hindered settling (Richardson & Zaki, 1954; Yin & Koch, 2007; Dey et al., 2019). Consequently, the mean fall velocity in a homogeneous suspension of spherical particles is less than the terminal velocity of a single isolated particle. The most widely used empirical relation between the hindered settling velocity U^* and volumetric particle concentration ϕ comes from sedimentation and liquid fluidization experiments, which showed that $U^* = U_t(1-\phi)^n$ (Richardson & Zaki, 1954), where U_t is the theoretical settling velocity of a single isolated particle in a pure fluid and n is a power-law exponent that depends on the particle Reynolds number $Re_p(U_t)$. For the range of Re_p in this study, the relevant hindered settling model includes a prefactor k yielding $U^* = kU_t(1-\phi)^n$ (Yin & Koch, 2007; Di Felice, 1999) and here $n = 4.4Re_p^{-0.1}$ (Richardson & Zaki, 1954). In order to test such a settling model, the data of U_m and ϕ_{Lm} are compared to an empirical expression $U_m = p_1(1-\phi_{Lm})^{p_2}$ which has a similar functional form to the hindered settling model.

For suspensions of 467 μm particles, the data are well described with $p_1 = kU_t = 2.9 \pm 0.1$ m/s and $p_2 = 4.89 \pm 2.5$ (Fig. 7c). For a single particle, $U_t \sim 3.5$ m/s, which implies that $k \sim 0.8$, in agreement with literature values (Yin & Koch, 2007; Di Felice, 1999). Moreover, the exponent obtained from the fit is very close to the improved relationship $n = (5.1 + 0.27 * Re_p^{0.9})/(1 + 0.1 * Re_p^{0.9})$, where Re_p is calculated from the theoretical settling velocity of a single particle (Garside & Al-Dibouni, 1977).

Hindered settling cannot account for the settling velocity increasing with the solid volume fraction in suspensions with 78 μm particles. Instead, this dependence may be captured by power law $U_m = p_3\phi_{Lm}^{p_4} + p_5$, with $p_3 = 2804$ m/s, $p_4 = 1.9 \pm 0.6$. Here $p_5 = 0.47 \pm 0.02$ m/s represents the single particle settling velocity in the limit of very low ϕ, which is higher than the predicted theoretical velocity for a single particle $U_t \sim 0.37$ m/s in the intermediate flow regime (Fig. 7a). A power law relation between the solid volume fraction and the settling velocity was also observed for volcanic ash particles (Del Bello et al., 2017). On the basis of this comparison, we argue that the settling dynamics in suspensions of small particles is to large extent controlled by the formation of particle clusters as discussed next.

4.2.4 Clustering

It is difficult to quantify the particle concentration in, and shape of, clusters due to the extensive light scattering by the particles, and the additional problem of interpreting a 2D projection of a 3D structure. Not withstanding these limitations, the cluster velocity appears to be well defined in the suspensions (Fig. 6 and supplementary movies). Analysis of the cluster trajectories suggests that the mean reduced settling velocity of clusters (i.e., $U_{cluster*}$ in the laboratory reference frame) is slightly lower in suspensions of 78 μm particles than in suspensions of 467 μm particles. However, the cluster velocity for settling in static air is $U_{cluster} = U_{cluster*} + U_m$ yielding $U_{cluster} \sim 0.9{+}0.7{=}$ 1.6 m/s and $U_{cluster} \sim 1.1{+}2.5{=}$ 3.6 m/s in suspension of 78 μm and 467 μm particles, respectively (Fig. 8).

To quantify the contribution of the clusters to the overall settling velocity of the mixture, we evaluate the ratio $U_{cluster}/U_t$. For the suspensions of 78 μm particles we find $U_{cluster}$ is about 4 times larger than U_t, resulting in a significant impact of clusters on the settling dynamics of the suspension (Fig. 8a). Instead, for the 467 μm particles the $U_{cluster} \sim U_t$, making it possible for hindered settling to dominate (which is a settling mechanism for isolated particles) (Fig. 8b).

The picture that emerges is the following. For suspensions of 78 μm particles, the bulk $Re \sim 1500$ implies a laminar flow. However, spatial fluctuations in the particle concentration may generate turbulence, an effect called cluster induced turbulence (CIT) (Capecelatro et al., 2015; Fong & Coletti, 2022). CIT occurs when the mass loading $\psi = \sigma\phi/(1{-}\phi) \gg 1$, which is the case here as $\psi \sim 10$. The elongate and apparently dense clusters have a higher settling velocity than individual particles, resulting in the increase of U_m with ϕ_{Lm}. In contrast, for the suspensions of larger particles, the bulk $Re \sim 6800$ implies turbulent flow. The decrease of U_m with increasing ϕ_{Lm} is well captured by a hindered settling model (Fig. 7c). Significant clustering is also observed in these suspensions, however, as the settling velocity of the clusters is not significantly different than that of a single particle, the clusters do not appear to impact the hindered settling mechanism. In other words, in suspensions of small particles the clusters dominate the settling dynamics, whereas the settling in suspensions of larger particles is dominated by hindered settling. The impact of clusters on particle settling may be related to the different shape, particle concentration, and longevity of the clusters, which in turn may depend on how particles are coupled to fluid motion (Nitsche & Batchelor, 1997; Pignatel et al., 2011; Chen et al., 2021).

The Stokes number captures the ability of particles to respond to changing flow conditions and is the ratio of the particle response time τ_p to a characteristic flow time scale τ_f (for the largest eddies $\tau_f = D/U_m$), so that

$$\mathrm{St} = \frac{(\rho_2 - \rho_1)d^2 U_m}{18\eta D}. \tag{4}$$

Clustering is sensitive to St (Bec, 2003). When St$\ll 1$ particles are well coupled to the flow and follow streamlines. When St$\gg 1$ particle motion is decoupled from turbulent motions. When St is of order 1, particles tend to accumulate at the edges of eddies (Maxey, 1987; Bec et al., 2007), leading to a local increase in particle concentration, a process that can initiate cluster formation. Our 78 μm particles at $U_m \sim 0.7$ m/s have St$=$ 0.8, and the $d = 467$ μm particles with $U_m \sim 2.5$ m/s have St$=$ 105 with the above definition of St, meaning that suspensions of smaller particles are more prone to clustering. Clusters of small particles may thus last longer and have higher particle concentrations, and consequently their $U_{cluster}$ and $U_{cluster}/U_m$ are larger than for clusters of high St particles. As a result, clustering may have a dominant role for the smaller particles, while hindered settling prevails for the larger particles. Future experiments and additional probing of particle concentration are needed to disentangle the role of the particle size and

the velocity profile on the persistence of clusters as well as cluster shape and concentration.

4.3 Geophysical implications

Our experiments show that the consequence of clusters on the settling velocity depends essentially on the Stokes number. Here, relative to the settling velocity of isolated particles U_t, our Stokes number O(1) particles settle with a mean velocity twice as large, and clusters of these particles have settling velocities that are even four times as large. However, our larger Stokes number O(10^2) particles experience hindered settling, with settling speeds up to 30% slower than U_t, while clusters in these suspensions have settling velocity roughly equal to U_t. These types of phenomena that arise from 4-way coupling are not accounted for in some models of particle transport used to simulate volcanic plumes, such as Ash3D (Schwaiger et al., 2012), TEPHRA (Bonadonna et al., 2005), FALL3D (Folch et al., 2020) and PLUME-MOM/HYSPLIT (Stein et al., 2015) that consider theoretical single-particle settling velocities. Modifications to the particle drag and settling velocity (Fig. 7) translate into additional uncertainty in such models. Settling velocities lower or higher than that of the theoretical velocities for single particles are a possible cause of discrepancy between simulated and observed fall deposit characteristics such as grain size and mass of deposit per unit area (Tadini et al., 2020). As highlighted in the report by the National Academies of Sciences, Engineering and Medicine (2017), particle-scale processes influence the large scale dynamics of volcanic eruptions. Similarly, in their review of pyroclastic density currents, and relevant to geophysical turbulent gas-particles mixtures in general, Lube et al. (2020) wrote “drag law correction and sub-grid models that account for mesoscale clustering must be developed” .

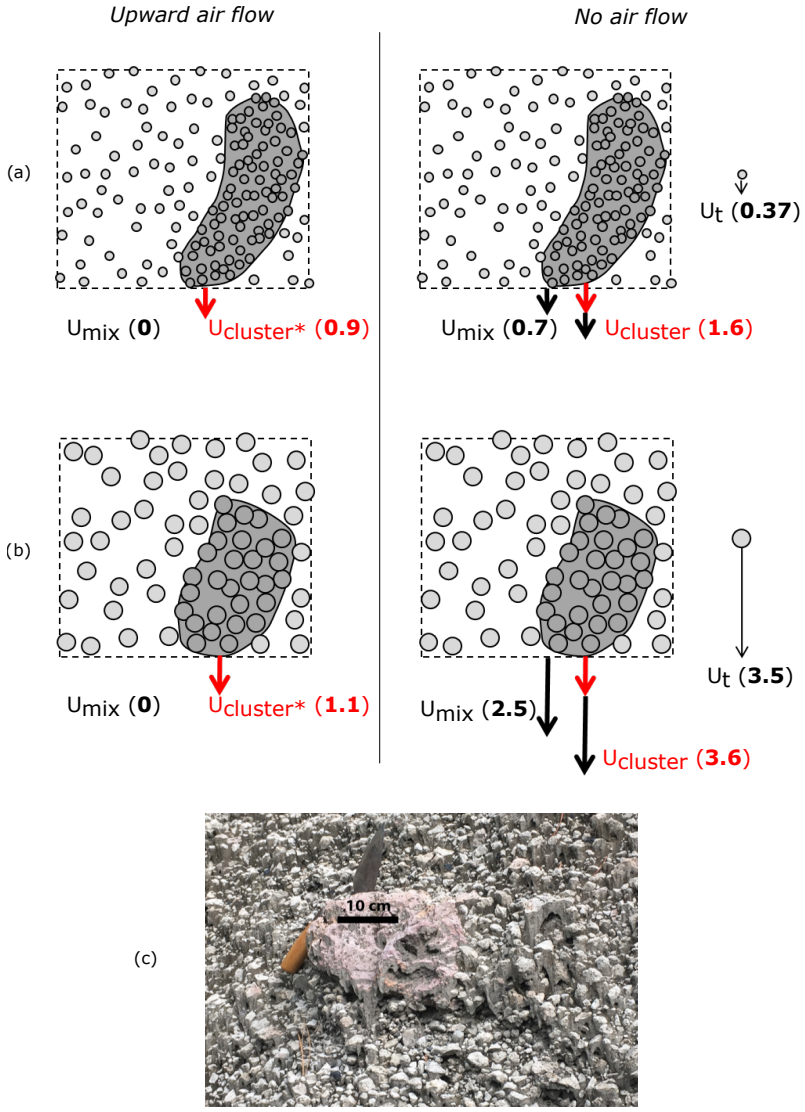


Figure 8. Schematic of the settling velocities (in m/s). (a) Suspensions of d= 78 μm particles. Left panel, settling velocities in the presence of an upward air flow (i.e., velocities in the laboratory reference frame). The mixture is suspended, while clusters settle at a reduced velocity. Right panel, settling in the absence of an air flow. The mixture settles with a velocity $U_{mix} \sim U_m$ and clusters settle at velocities $\sim U_m + U_{cluster^*}$. For comparison the terminal settling velocity U_t of a single particle in the intermediate regime is also illustrated. Note that this velocity is significantly less than the settling velocity of the mixture and the clusters. (b) Suspensions of d= 467 μm particles. In this case, the settling velocity of the mixture is less than the theoretical settling velocity of a single particle in the intermediate flow regime. (c) Dacite pumice fall from the 10.5 ka Plinian eruption of Llaima, Chile (Northing 570558, Easting 0271863; photo taken 7 January 2020).

One fall deposit characteristic from volcanic plumes that might result from clustering, and be diagnostic that clustering is an important process in spreading umbrella clouds, is the occurrence of unusually large clasts in an otherwise well-sorted deposit. As an illustrative example, we consider the dacite pumice fall from the 10.5 ka Plinian erup-

tion of Llaima, Chile (Schindlbeck et al., 2014). Fig. 8c shows unit IIIb of the deposit, 12 km from the vent. Notable is the outsized clast in a matrix of smaller pumice (most of the deposit consists of cm size lapilli with a small proportion of large clasts). The intermediate diameter of the large clast, measured with a ruler, is 16 cm. The median diameter of the pumice, measured by dry sieving in the lab, is 1 cm with an Inman sorting value of 0.45 (see Supplementary Information section 3 for details). 12 km is too distal for the large clast to be a ballistic bomb. Our hypothesis is that within the spreading umbrella cloud, the lapilli settled in clusters with a similar settling velocity as the large particle since they were deposited together. We assume that U_m is equal to the fall velocity of the coarsest particles. For the large and median particle sizes, diameters of 16 and 1 cm respectively, the theoretical settling speeds assuming a density of 600 kg/m^3 are ∼61 m/s and ∼14 m/s using the Abraham (1970) drag model. This implies a roughly 4-fold increase in settling speed for the clusters of small particles, which is similar to the enhanced settling speed in our experiments (Fig. 8) and mesoclusters in large scale density current experiments (Breard et al., 2016).

More generally in volcanic plumes and spreading umbrella clouds, enhanced (or hindered) settling can cause deposits with mass per unit area larger (or smaller) and grain sizes smaller (or larger) than expected for single size particles (Tadini et al., 2020, 2022; Freret-Lorgeril et al., 2020; Gilchrist & Jellinek, 2021). Clustering in mixtures containing particles with Stokes number O(1) is an alternative to ash aggregation commonly assumed in simulations to explain enhanced settling (e.g., Tadini et al., 2022). The fact that bimodal fallout deposits, such as the one at Llaima (Fig. 8), are relatively rare suggests effective particle size segregation occurs near the vent in most cases. On the other hand, hindered settling accounts for reduced particle settling velocity, otherwise explained by non spherical particle shape or the presence of wind (Marchetti et al., 2022). In a broader context, hindered settling is likely to occur in various types of geophysical flows containing particles with Stokes number $\gg 1$, and our experiments suggest that this mechanism can operate at concentrations as low as ~ 1 vol.%, which may be surprising.

Numerical simulations of pyroclastic currents showed that unrealistically high particle drag coefficients, at least 30 times larger than commonly estimated for typical volcanic particles ($\sim 0.5-1$), were required to match the runout distance of the ash-cloud surges at Merapi, 2010 (Kelfoun et al., 2017) and Mount Pelée (Martinique), May 8th, 1902 (Gueugneau et al., 2020). To explain the high drag coefficient, Gueugneau et al. (2020) concluded that hindered settling occurred as a consequence of the increase in particle concentration towards the lower part of the currents, our experimental findings support this statement. Even though it is unlikely that hindered settling alone can account for the large discrepancy between their simulation and the natural case, it may be partly responsible. Our experiments showing hindered settling provide insights into the possible settling characteristics of the particles in the basal layer of these natural flows, that is, with Stokes numbers $\gg 1$ and at concentrations as low as ~ 1 vol.%.

5 Conclusion

We measured the local solid volume fraction in dilute suspensions of glass particles in air using two independent techniques, acoustic probing and local fluid pressure measurements. We showed that these techniques yield similar solid volume fractions, thus providing two attractive tools to investigate optically opaque mixtures in analogue laboratory experiments. We anticipate that a combination of these techniques may be useful if, for example, both the particle concentration and particle size are not known. Indeed, the local pressure measurements may then be used to obtain a solid volume fraction, which could be used in the sound attenuation calculation to obtain the particle size.

Our experiments in a vertical pipe demonstrate that the local particle concentration in dilute suspensions depends on the initial amount of particles, the particle size,

and the air flow velocity. In suspensions of 78 μm particles, higher air velocities were needed to obtain higher local particle concentrations and we argue this was due to the presence of clusters that settled faster than individual particles. In contrast, in suspensions of 467 μm particles, higher local particle concentrations were achieved at lower air velocities as a consequence of hindered settling of the particles, despite the presence of clusters. Differences in the shape and particle concentration of the clusters may explain their different settling behaviours.

Our results have implications for modeling geophysical dilute gas-particle mixtures. The field example we discuss suggests that in volcanic plumes clusters of relatively small particles have enhanced settling velocities, similar to that of larger clasts, decreasing the sorting in fall deposits. Other geophysical flows with particles of broad grain size ranges are likely to exhibit similar flow dynamics. We conclude that the formation of clusters and their settling velocities being significantly different than that of single particles should be considered in models of geophysical processes through drag law corrections.

6 Acknowledgement

We thank B. Andrews, A. Marshall, B. Brand, G. Giordano, and P. Valdivia for field sampling, discussions, and ideas about the deposit pictured in Figure 8. We thank X. Jia for valuable discussions on sound attenuation. This project is part of a program of the International Research Center of Disaster sciences and sustainable Development at University Clermont Auvergne. This is Laboratory of Excellence ClerVolc contribution n○ XXX. M.M. is supported CIFAR Earth 4D and NSF 2042173.

7 Open Research

Datasets and a short description for this research are available with DOI: 10.5281/zenodo.7565085 on https://doi.org/10.5281/zenodo.7565085.

References

Abraham, F. F. (1970). Functional dependence of drag coefficient of a sphere on reynolds number. *The Physics of Fluids*, *13*, 2194.

Allegra, J. R., & Hawley, S. A. (1972). Attenuation of sound in suspensions and emulsions: Theory and experiments. *Journal of the Acoustical Society of America*, *51*, 1545-1564.

Bagheri, G. H., Bonadonna, C., Manzella, I., & Haas, P. (2013). Dedicated vertical wind tunnel for the study of sedimentation of non-spherical particles. *Rev. Sci. Instr.*, *84*, 054501.

Bec, J. (2003). Fractal clustering of inertial particles in random flows. *Physics of Fluids*, *15*, L81.

Bec, J., Biferale, L., Cencini, M., Lanotte, A., Musacchio, S., & Toschi, F. (2007). Heavy particle concentration in turbulence at dissipative and inertial scales. *Physical Review Letters*, *98*, 084502.

Berruti, F., Pugsley, T. S., Godfroy, L., Chaouki, J., & Patience, G. S. (1995). Hydrodynamics of circulating fluidized bed risers: a review. *The Canadian Journal of Chemical Engineering*, *73*, 579-602.

Bonadonna, C., Philips, J. C., & Houghton, B. F. (2005). Modeling tephra sedimentation from a ruapehu weak plume eruption. *Journal of Geophysical Research*, *110*, B08209.

Bonadonna, C., & Phillips, J. C. (2003). Sedimentation from strong volcanic plumes. *J. Geophys.Res.*, *108*, 2340.

Brandt, L., & Coletti, F. (2022). Particle-laden turbulence: Progress and perspectives. *Annual Review of Fluid Mechanics*, *54*, 159–189.

Breard, E. C. P., Lube, G., Jones, J. R., Dufek, J., Cronin, S. J., Valentine, G. A., & Moebis, A. (2016). Coupling of turbulent and non-turbulent flow regimes within pyroclastic density currents. *Nature Geoscience*, *9*, 767– 771.

Cahyadi, A., Anantharaman, A., Yang, S., Karri, S. R., Findlay, J. G., Cocco, R. A., & Chew, J. W. (2017). Review of cluster characteristics in circulating fluidized bed (cfb) risers. *Chemical Engineering Science*, *158*, 70-95.

Capecelatro, J., Desjardins, O., & Fox, R. (2015). On fluid–particle dynamics in fully developed cluster-induced turbulence. *J. Fluid Mech.*, *780*, 578-635.

Challis, R. E., Povey, M. J. W., Mather, M. J., & Holmes, A. K. (2005). Ultrasound techniques for characterizing colloidal disperions. *Reports on progress in physics*, *68*, 1514-1637.

Chen, P., Chen, S., Yang, M., & Li, S. (2021). Falling clouds of particles with finite inertia in viscous flows. *Physics of Fluids*, *33*, 033314.

Del Bello, E., Taddeucci, J., de' Michieli Vitturi, M., Scarlato, P., Andronico, D., Scollo, S., ... Ricci, T. (2017). Effect of particle volume fraction on the settling velocity of volcanic ash particles: Insights from joint experimental and numerical simulations. *Scientific Reports*, *7*, 39620.

Dey, S., SK, A. Z., & E., P. (2019). Terminal fall velocity: the legacy of stokes from the perspective of fluvial hydraulics. *Proc. R. Soc. A*, *475*, 20190277.

Di Felice, R. (1999). The sedimentation velocity of dilute suspensions of nearly monosized spheres. *Int. J. Multiphase Flow*, *25*, 559.

Epstein, P. S., & Carhart, R. R. (1953). The absorption of sound in suspensions and emulsions. i. waterfog in air. *Journal of the Acoustical Society of America*, *25*, 553-565.

Folch, A., Mingari, L., Gutierrez, N., Hanzich, M., Macedonio, G., & Costa, A. (2020). Fall3d-8.0: a computational model for atmospheric transport and deposition of particles, aerosols and radionuclides – part 1: Model physics and numerics. *Geoscientific Model Development*, *13*, 1431–1458.

Fong, K. O., & Coletti, F. (2022). Experimental analysis of particle clustering in moderately dense gas-solid flow. *J. Fluid Mech.*, *933*, A6.

Fornari, W., Picano, F., Sardina, G., & Brandt, L. (2016). Reduced particle settling speed in turbulence. *J. Fluid Mech.*, *808*, 153-167.

Fornari, W., Zade, S., Brandt, L., & Picano, F. (2019). Settling of finite-size particles in turbulence at different volume fractions. *Acta Mech*, *230*, 413-430.

Freret-Lorgeril, V., Gilchrist, J., Donnadieu, F., Jellinek, A. M., Delanoë, J., Latchimy, T., ... S., V. (2020). Ash sedimentation by fingering and sediment thermals from wind-affected volcanic plumes. *Earth and Planetary Science Letters*, *534*, 116072.

Fullmer, W. D., & Hrenya, C. M. (2017). The clustering instability in rapid granular and gas-solid flows. *Annual review of fluid mechanics*, *49*, 485-510.

Garside, J., & Al-Dibouni, M. R. (1977). Velocity-voidage relationships for fluidization and sedimentation in solid-liquid systems. *Ind.Eng Chem. Proc. Des. Dev.*, *16*, 206-214.

Gilchrist, J. T., & Jellinek, A. M. (2021). Sediment waves and the gravitational stability of volcanic jets. *Bull Volcanol*, *83*, 64.

Gueugneau, V., Kelfoun, K., Charbonnier, S., Germa, A., & Carazzo, G. (2020). Dynamics and impacts of the may 8th, 1902 pyroclastic current at mount pelée (martinique): New insights from numerical modeling. *Frontiers in Earth Science*, *8*, 279.

Jessop, D. E., & Jellinek, A. M. (2014). Effects of particle mixtures and nozzle geometry on entrainment into volcanic jets. *Geophysical Research Letters*, *14*, 060059.

Kelfoun, K., Gueugneau, V., Komorowski, J. C., Aisyah, N., Cholik, N., & Merciecca, C. (2017). Simulation of block-and-ash flows and ash-cloud surges of the 2010 eruption of merapi volcano with a two-layer model. *Journal of*

Geophysical Research: Solid Earth, *122*, 4277–4292.

Lube, G., Breard, E., Esposti-Ongaro, T., Dufek, J., & Brand, B. (2020). Multiphase flow behaviour and hazard prediction of pyroclastic density currents. *Nature Reviews Earth & Environment*, *1*, 348–365.

Marchetti, E., Poggi, P., Delle Donne, M., D.and Pistolesi, Bonadonna, C., Bagheri, G., Pollastri, S., ... Ripepe, M. (2022). Real-time tephra-fallout accumulation rates and grain-size distributions using asher (ash collector and sizer) disdrometers. *Journal of Volcanology and Geothermal Research*, *429*, 107611.

Maxey, M. R. (1987). The gravitational settling of aerosol particles in homogeneous turbulence and random flow fields. *Journal of Fluid Mechanics*, *174*, 441-465.

National Academies of Sciences, Engineering and Medicine. (2017). *Volcanic eruptions and their repose, unrest, precursors, and timing.* Washington DC: The National Academies Press.

Nielsen, P. (1993). Turbulence effects on the settling of suspended particles. *J. Sediment. Petrol*, *63*, 835-838.

Nitsche, J. M., & Batchelor, G. K. (1997). Break-up of a falling drop containing dispersed particles. *J. Fluid Mech.*, *340*, 161-175.

Pierce, A. D., Siegmann, W. L., & Brown, E. (2016). Suspension theory for the effect of silt particles on attenuation of the compressional waves in marine mud sediments. *Proc. Mtgs. Acoust.*, *29*, 005003.

Pignatel, F., Nicolas, M., & Guazzelli, E. (2011). A falling cloud of particles at a small but finite reynolds number. *J. Fluid Mech.*, *671*, 34-51.

Rhodes, M. (2008). *Introduction to particle technology, second edition.* West Sussex, England: John Wiley & Sons, Ltd.

Richardson, J. F., & Zaki, W. N. (1954). Sedimentation and fluidisation, part i. *Trans. Inst. Chem. Eng.*, *32*, 35-53.

Schindlbeck, J. C., Freundt, A., & Kutterolf, S. (2014). Major changes in the post-glacial evolution of magmatic compositions and pre-eruptive conditions of llaima volcano, andean southern volcanic zone, chile. *Bulletin of Volcanology*, *76*, 830.

Schwaiger, H. F., Denlinger, R. P., & Mastin, L. G. (2012). Ash3d: A finite-volume, conservative numerical model for ash transport and tephra deposition. *Journal of Geophysical Research*, *117*, B04204.

Steger, C. (1998). An unbiased detector of curvilinear structures. *EEE Trans. Pattern Anal. Mach. Intell.*, *20*, 113-125.

Stein, R. R., A. F.and Draxler, Rolph, G. D., Stunder, B., Cohen, M. D., & Ngan, F. (2015). Noaa's hysplit atmospheric transport and dispersion modeling system. *Bulletin of the American Meteorological Society*, *96*, 2059-2078.

Tadini, A., Gouhier, M., Donnadieu, F., de' Michieli Vitturi, M., & Pardini, F. (2022). Particle sedimentation in numerical modelling: A case study from the puyehue-cordón caulle 2011 eruption with the plume-mom/hysplit models. *Atmosphere*, *13*, 784.

Tadini, A., Roche, O., Samaniego, P., Guillin, A., Azzaoui, N., Gouhier, M., ... Le Pennec, J. L. (2020). Quantifying the uncertainty of a coupled plume and tephra dispersal model: Plume-mom/hysplit simulations applied to andean volcanoes. *Journal of Geophysical Research*, *125*, 1-20.

Tsuji, Y., Morikawa, Y., & Hiroshi, S. (1984). Ldv measurements of an air-solid two-phase flow in a vertical pipe. *J. Fluid Mech.*, *139*, 417-434.

Uhlmann, M., & Doychev, T. (2014). Sedimentation of a dilute suspension of rigid spheres at intermediate galileo numbers: the effect of clustering upon the particle motion. *J. Fluid Mech.*, *752*, 310-348.

Urick, R. J. (1948). The absorption of sound in suspensions of irregular particles. *Journal of the Acoustical Society of America*, *20*, 283-288.

van den Wildenberg, S., Jia, X., & Roche, O. (2020). Acoustic probing of the particle concentration in turbulent granular suspensions in air. *Scientific Reports*,

10, 16544.

Wang, L. P., & Maxey, M. R. (1993). Settling velocity and concentration distribution of heavy particles in homogeneous isotropic turbulence. *J. Fluid Mech.*, *256*, 27-68.

Weit, A., Roche, O., Dubois, T., & Manga, M. (2019). Maximum solid phase concentration in geophysical turbulent gas-particle flows: Insights from laboratory experiments. *Geophysical Research Letters*, *46*, 6388-6396.

Yin, X., & Koch, D. L. (2007). Hindered settling velocity and microstructure in suspensions of solid spheres with moderate reynolds numbers. *Phys. Fluids*, *19*, 093302.

Ying, C. F., & Truell, R. (1956). Scattering of a plane longitudinal wave by a spherical obstacle in an isotropically elastic solid. *Journal of applied physics*, *27*, 1086-1097.